Hydrodynamic loading of perforated disks in creeping flows

E. F. Strong,[1] M. Pezzulla,[2] F. Gallaire,[3] P. Reis,[2] and L. Siconolfi[3,*]

[1]*Department of Mechanical Engineering, Massachusetts Institute of Technology, Cambridge, Massachusetts 02139, USA*

[2]*Flexible Structures Laboratory, École Polytechnique Fédérale de Lausanne, 1015 Lausanne, Switzerland*

[3]*Laboratory of Fluid Mechanics and Instabilities, École Polytechnique Fédérale de Lausanne, 1015 Lausanne, Switzerland*

(Received 25 January 2019; published 6 August 2019)

We present results from an experimental investigation of a viscous fluid driven through and around porous disks at low and moderate Reynolds number conditions: Re $= O(10^{-4}$–$10^{-3})$ and Re $= O(1$–$10)$. Specifically, we quantify the hydrodynamic drag that these thin circular disks exhibit as a function of their size and the shape of their voids, while keeping their porosity fixed (void fraction, $\phi = 0.69 \pm 0.02$). We characterize the hydrodynamic loading using the drag ratio, which compares the magnitudes of drag experienced by a porous disk versus that of an impermeable, but otherwise equivalent, reference disk. We find that this drag ratio depends on the effective void radius, but not on the thickness of the disk. During this analysis, great attention has been dedicated to properly account for the effect of the wall confinement on the experimental data. Through scaling analysis, we rationalize our results by comparing them to an existing analytical solution for flow through and around porous disks. In particular, we find that an existing model based on Darcy flow within the porous disk and on Stokes flow outside the disk can be used in conjunction with a permeability model based on aperture flow to predict the forces that porous disks experience, even though the disks have finite thickness. Ultimately, we are able to combine these existing models to successfully predict the dependence of our experimentally measured drag ratio as a function of the Brinkman parameter of the perforated disks, at a fixed level of porosity. In contrast to the sedimentation experiments that are typically employed to evaluate the geometrical effects on the drag forces experienced by objects at low Re, our experiments were displacement controlled.

DOI: 10.1103/PhysRevFluids.4.084101

I. INTRODUCTION

Low Reynolds (Re) number flows through and around porous objects and conglomerates of particles arise in a variety of natural and technological scenarios, in contexts ranging from marine life and ecosystems [1–9] to wastewater treatment [10]. Being able to predict how the fluid flow depends on the geometry, porosity, and permeability of these objects is a challenging endeavour given the nontrivial and nonlinear couplings at play. Still, there are numerous biological examples in low Re environments where these mechanisms are naturally exploited. For example, barnacles alter the way they use their thin, featherlike thoracic appendages to capture food depending on the fluid flow [3,8]. Spiny lobsters flick their hairy antennules at two different speeds to facilitate olfaction by first holding water between their hairs long enough for sensing, and then releasing the sample [1]. In terrestrial environments, wasps may be able to modulate the behavior of their porous,

*siconolfi.lorenzo@gmail.com

bristled wings to act like solid wings by decreasing the angle of attack [11]. In a different context, the porous structures of pollen, both in the atmosphere [12] and underwater [13], must be taken into account when analyzing how and how far these particles travel.

Beyond biological systems, developing an understanding of the behavior of thin, porous structures has applications in a variety of other fields. For example, earlier efforts in this field have enabled predictions for the time it takes for marine snow to settle in the ocean, an important parameter used to model the Earth's carbon cycle [4]. Moreover, many wastewater treatment facilities rely on flocculation as one of several steps to reduce the turbidity of water and return it to a clean condition; predicting the duration of this step is important in the design of the process [10]. Low Re number flow through and around porous objects is also relevant when the structures are thin and planar, as is the case with snowflakes and ice crystals [14,15]. Predicting the forces that these objects experience is critical to understand the terminal velocities of crystals in the atmosphere, a metric which climatologists use to model radiative transfer in climate models [16,17].

To address this class of problems of low Re number flows through and around porous structures, much work has been done through theory [18–23], computer simulations [24,25], and experiments [26–28]. However, these studies are mainly focused on flows through spheres or spheroids, and little attention has been given to the specific problem of flow through and around other slender, porous objects. Since it is precisely in these low Re conditions that many terrestrial and aquatic organisms exist [29,30], understanding how they function and how they influence their ecosystem requires knowing how their environments influence their behavior. The degree to which a fluid can move both *around* and *through* thin porous objects strongly affects the hydrodynamic drag, but in ways that are challenging to predict. For example, the porous wings of some insects, such as the *Mymaridae* (fairyfly) [31], comprise an intricate structure of bristles emanating from an inner core. Despite the relatively large porosity of this structural layout, the wings can generate sufficient lift to sustain the weight of the insect and enable a rich flight dynamics [32]. However, a predictive description of this process is yet to be uncovered [11]. This is one of many examples where understanding the locomotion of small-scale biological systems may, in the future, be informed by fundamental studies of flow through porous structures, which is the focus of the present investigation.

When studying the effect of porosity on the drag that a porous object experiences while traveling through a viscous fluid, at low Re numbers, it is customary to seek to establish a relationship between the characteristic geometric parameters of the object (e.g., porosity or, equivalently, void fraction ϕ; permeability k; and size l) and changes in the drag relative to the loading of an impermeable, but otherwise equivalent (density, geometry) reference object. For a fixed porosity, the effect of the geometric parameters is encapsulated in the *Brinkman parameter* [18], defined as

$$\beta = \sqrt{\frac{l^2}{k}}, \tag{1}$$

where l^2 represents a characteristic area of the object and k is its permeability, which describes the nature (e.g., density, connectivity, and tortuosity) of the pore structure in the object. When k is large, the network of pores offers little resistance to a fluid passing through them. In contrast, when k is small, the resistance is high. In turn, when β is large, the porous object behaves as if it were impermeable. For small β, the effect of the porosity of the object must be considered. The determination of β is typically accomplished through approximations using empirical relations between the porosity and structure of a substrate to its permeability such as the Davies correlation [33] or the Carman-Kozeny equation [34–36], or inferred based on the pressure drop experienced by a fluid across a sample of the porous material, measured in independent experiments [37].

The Brinkman parameter serves as the independent parameter in the drag ratio,

$$\Omega(\beta) = \frac{F_d(\beta)}{F_r}, \tag{2}$$

which quantifies the ratio between the drag force experienced by the porous object, F_d, and that by the reference object, F_r. We note that given that inertia is not relevant in the low Re regime, a corresponding expression for the drag ratio can be defined using the ratio of the terminal velocity of the reference object, U_r, to that of the porous object, U_p, such that $\Omega = U_r/U_p$. In the low Re numbers limit, the drag force is indeed proportional to the terminal velocity. Intuitively, when β is high (k is small compared to l^2), Ω should approach unity and the porous object behaves as if it were impermeable. On the other hand, when β is small (k is large compared to l^2), Ω should tend to zero since the fluid can pass through the object almost unencumbered.

Analytical treatments of flow through porous objects tend to involve segmenting the flow into two domains that are modeled separately: (1) the clear fluid *around* and (2) the fluid that flows *through* the porous object. The solutions of the two domains are then related to each other via appropriate interface conditions at the boundaries of the two regions.

In the outer domain, the dynamics of a Newtonian viscous fluid at low Re number is well described by the incompressible Stokes equations,

$$\nabla P = \mu \nabla^2 \boldsymbol{U}, \quad \nabla \cdot \boldsymbol{U} = \boldsymbol{0}, \tag{3}$$

where the gradients of the pressure, P, are balanced by the diffusion of velocity, $\boldsymbol{U}$, scaled with the dynamic viscosity μ.

Throughout this paper, we shall refer to three classical analytical solutions of the system (3) for the evaluation of the forces on impermeable bodies (hereafter called *reference bodies*), which are reviewed next. (i) The first, the Stokes formula derived by Stokes himself in 1851 [38], provides a prediction for the hydrodynamic drag $\boldsymbol{F}_{s,\infty}$ experienced by a sphere of radius r that is translating with a velocity $\boldsymbol{V}$ through a fluid with viscosity μ:

$$\boldsymbol{F}_{s,\infty} = -6\pi\mu r \boldsymbol{V}. \tag{4}$$

(ii) The second result is the drag force on a disk of radius r and with infinitesimal thickness, again in motion with velocity $\boldsymbol{V}$ through a fluid with viscosity μ,

$$\boldsymbol{F}_{d,\infty} = -16\mu\, r \boldsymbol{V}, \tag{5}$$

which was first obtained by Sampson in 1891 [39] and then experimentally verified by Squires and Squires [40]. (iii) The third case considers a flat annular disk of external radius r and internal radius r_i with infinitesimal thickness that translates with velocity $\boldsymbol{V}$ in a viscous fluid (see, for example, [41]). In particular, following [42], for a small internal radius, i.e., $r_i \ll r$, the drag of the annular disk can be evaluated as

$$\boldsymbol{F}^{\text{hole}}_{a,\infty} = -16\mu\, r \boldsymbol{V}\left(1 - 4r_i^3/3\pi^2 r^3\right), \tag{6}$$

whereas, in the limit of $r_i \to r$, the force can be approximated as

$$\boldsymbol{F}^{\text{ann}}_{a,\infty} = -16\mu\, r \boldsymbol{V}\{\pi^2/[(2+\epsilon)\ln(32/\epsilon) + \epsilon]\}, \tag{7}$$

where $\epsilon = -1 + r/r_i$. It is interesting to note that the force $\boldsymbol{F}^{\text{ann}}_{a,\infty}$ decreases weakly as the size of the internal hole increases, owing to the fact that the drag is mainly due to the pressure jump in the outer region of the annular disk. For example, if we consider a disk with $r_i = 0.8r$, the corresponding drag force is $\boldsymbol{F}^{\text{ann}}_{a,\infty} \approx 0.884\, \boldsymbol{F}_{d,\infty}$.

Modeling the flow within the porous domain is more nuanced and is typically accomplished using models based on Darcy's Law. This equation, initially developed by Darcy in 1856 to empirically study the fluid flow through gravel at a local wastewater treatment plant [43], then subsequently derived formally using a volume average scheme of the Stokes equations [44,45], has since become the standard first-order model for flow through porous media in fields ranging from geology to biology [37]. Darcy's Law can be written as

$$-\nabla P = \frac{\mu}{k} \langle \boldsymbol{U} \rangle, \quad \nabla \cdot \langle \boldsymbol{U} \rangle = \boldsymbol{0}, \tag{8}$$

where the pressure drop ∇P across a statistically homogeneous and isotropic porous media is related to the mean velocity of the fluid, $\langle \boldsymbol{U} \rangle$, traveling through the porous media by way of a proportionality constant μ/k. This constant reflects the resistance that the fluid experiences due to the combined effect of the dynamic viscosity of the fluid, μ, and the permeability of the media, k. This model has been largely studied and improved by including terms to take into account, for example, the diffusion and the convection inside the porous media (see [45,46]). However, when we consider the dynamics of thin objects in viscous fluids at low Reynolds numbers, these effects can be considered negligible and Darcy's approximation gives a good description of the flow inside the porous media. Specifically, the solution for the flow past a porous disk of infinitesimal thickness has been analytically derived by Vainshtein [22], by coupling the Stokes (3) and Darcy (8) systems, leading to a formula for the drag ratio that can be written as

$$\Omega = \frac{\pi \beta^2}{\pi \beta^2 + 1}, \tag{9}$$

where $\beta = \sqrt{rt/k}$, for disk radius r and thickness t. This solution was calculated by analyzing the flow around and through a porous spheroid in the limit of infinitesimal thickness [22], taking as interface conditions at the fluid-solid boundaries the continuity of the velocity, as well as that of pressure at the stagnation point alone—exploiting the symmetries of the spheroid [22].

In the present study, starting from Eq. (9), we now ask if it is possible to derive a more practical relation that links the drag ratio Ω directly to the geometrical characteristics of the voids. Specifically, instead of studying a generic homogeneous porous disk, we consider a disk whose permeability is due to the presence of through-thickness circular holes. We seek to have a predictive description for the drag ratio of the perforated disk, once the characteristics of the holes pattern are given. Here, we address the above question experimentally by focusing on the hydrodynamic drag exerted by a viscous fluid on broadwise translating perforated disks in the limit of low Re numbers. Keeping the porosity constant, while varying the holes' size and number, the experimental measurements of the forces involved enable us to derive the behavior of the drag as a function of permeability. Furthermore, we also carry out dedicated numerical simulations to support the experimental activities, in particular to take into account the effect of wall confinement on the flow behavior when permeable disks are considered. We highlight that our experiments are performed under imposed displacement conditions, in contrast to past sedimentation studies. We argue that displacement control is more amenable to precision systematic experimentation given that the results do not depend on the relative densities of the solid and the fluid.

Our paper is outlined as follows. In Sec. II, we introduce our apparatus and present the experimental protocol. The results of our study are then reported in Sec. III. First, we benchmark our experiment with existing solutions by systematically measuring the forces experienced by unperforated (reference) disks over a range of radii, at low and moderate Re numbers (Sec. III A). The results of this experiment demonstrate that our experimental protocol and analysis methods yield results consistent with those in the literature. Next, we shift to porous disks and quantify the effect of void size on the drag ratio (Sec. III B). Then, the results of the numerical simulations are described and discussed in comparison with the experimental ones in Sec. III C. In Sec. IV, we seek to rationalize our results via a scaling analysis coupled with the theoretical result for flow through and around a porous disk given in Eq. (9) by Ref. [22], demonstrating that our results are consistent with this solution. Lastly, in Sec. V, we conclude by discussing the implications of our findings and we detail paths for future work. In Appendices A and B, we detail the experimental protocol used to measure the viscosity of the fluids and the calibration of the force on the supporting rods, respectively.

II. EXPERIMENTS

In this section, we introduce the experimental apparatus and present the protocol followed to measure the drag force that a perforated disk experiences while pushed through a bath of viscous

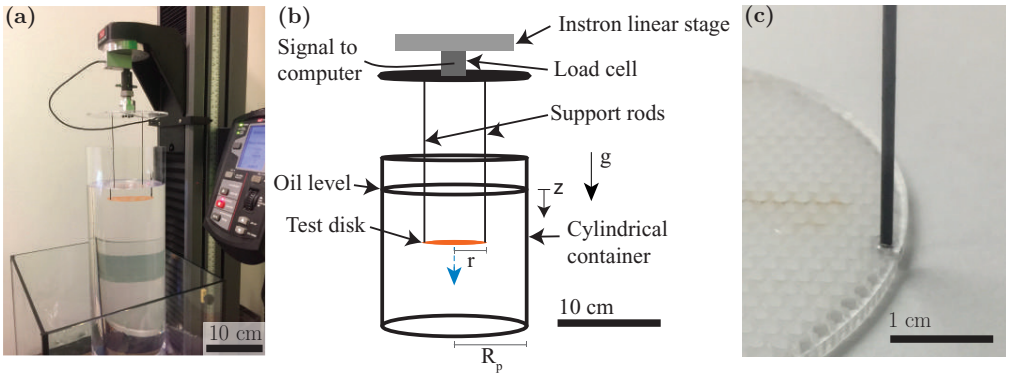

FIG. 1. Experimental apparatus. (a) Photograph and (b) schematic of the experimental setup. An Instron universal testing machine was used to drive disks with radius r and thickness t, with or without voids (Fig. 2), through an oil bath. This oil had viscosity μ and was contained in a pipe with cylindrical radius R. The disks were driven at a range of speeds, U, and the force the system experienced was recorded by a load cell on the linear stage. The disks were supported by two slender vertical rods, melted to them and press fit into a holder attached to the UTS. (c) Representative photograph of the detail of the joint between the support rod and the disk specimen.

fluid, under imposed displacement conditions. We have systematically studied the dependence of the drag ratio of a thin perforated disk of radius r and thickness t (with $t < 0.025r$) on the characteristic size of its voids, a, while driving it through a cylindrical column of a viscous oil.

A. Experimental apparatus

In Fig. 1(a), we present a photograph of our experimental apparatus, comprising a cylindrical column of oil through which a universal testing machine (Instron 5943, hereafter referred to as UTS) drove the disk specimens. The samples were connected to the load cell (10 N, 2530 series, Instron) of the UTS with two slender Nitinol rods (radius $R_r = 0.28$ mm, length $l = 16.0$ cm). The oil container was a cast acrylic pipe (McMaster-Carr, $R_p = 7.0$ cm inner radius) sealed at its bottom with a silicone-oil-based polymer (Vinyl Polysiloxane, Elite Double 32, Zhermack). Experiments were conducted in two different viscous fluids: (1) mineral oil (Crystal Plus Food Grade 500FG, STE Oil Company, Inc.) and (2) silicone oil (DMS-T51, Gelest). The characteristics of these fluids (dynamic viscosity and density) are discussed in Appendix A. In short, the mineral and silicone oils had viscosities of the order of 0.1 and 100 Pa s, respectively, the exact values of which were temperature dependent [Fig. 11 and Eq. (A1)]. The corresponding densities were $\rho_1 = 868$ kg/m^3 (for the mineral oil) and $\rho_2 = 977$ kg/m^3 (for the silicone oil). A different container was used for each of the two types of oil used and the heights of these containers were $h_1 = 26.0$ cm (for the mineral oil) and $h_2 = 51.0$ cm (for the silicone oil).

The coordinate system used to describe our experiments has a vertical z direction that originates at the free surface of the oil and is oriented downwards [Fig. 1(b)]. All experiments were conducted within the region $30 \leqslant z \leqslant 180$ mm, where the effects of the free surface and the floor were found to be negligible. The disk specimens were set concentrically to within 0.07% of the radius of the container.

The tips of two Nitinol rods that supported the disks [see Fig. 1(c)] were heated over the flame of a disposable lighter up to approximately 300 °C, and were then pressed vertically into the disk, $180 \pm 1^\circ$ apart, and 0.2 ± 0.1 mm from the edge of the disk. Once the locally melted plastic solidified, the rods were fixed vertically into the disk and a speck of superglue was applied to enforce clamping. The opposite end of each Nitinol rod was press fit into a predrilled hole on a 6.35-mm-thick acrylic plate that was itself rigidly attached to the load cell.

The tilt of the disk was minimized by ensuring it was leveled with respect to the free surface of the bath in two ways. First, the initial contact that the test sample made with the free surface as it was lowered from above into the oil was monitored visually. With no tilt, the entire disk should simultaneously touch the fluid. Second, the test sample was raised out of the oil bath and the disk was deemed leveled if oil flowed off at the center of the disk (instead of from its edge). If the initial contact occurred progressively from one side of the disk towards the other or the oil did not pool on the surface of the disk, the support rods were reattached to the sample.

During an experimental test, the UTS drove the specimen through the fluid while its load cell recorded the force experienced by the system. This force signal was acquired every 10^{-4} mm and at every change in $F = 10^{-4}$ N, corresponding to rates of approximately 20–80 Hz, depending on the experiment. The tare force was referenced to the stationary force at $z_0 = z(t = 0) = 30$ mm, so as to account for the apparent weight of the disk and the rods at this starting position. No out-of-plane disk oscillations were observed during the experiments.

B. Fabrication of the experimental samples: Continuous and perforated disks

The thin disks used in the experiments were fabricated by laser cutting sheets of either polyethylene terephthalate glycol shim stock (PETG, the ARTUS Corporation) or cast acrylic (McMaster-Carr). The thicknesses of the PETG sheets were $t = \{0.40,\ 0.50,\ 0.80,\ 1.30\} \pm 0.01$ mm and the thicknesses of the cast acrylic sheets were $t = \{1.55,\ 2.00,\ 3.00,\ 3.23\} \pm 0.01$ mm. Continuous disks with $t = 0.80 \pm 0.01$ mm were fabricated with radii varying in the range $12.7 \pm 0.1 \leqslant r \leqslant 52.5 \pm 0.1$ mm (11 values). The radii of all other disks were $r = 32.5 \pm 0.01$ mm. We define the void fraction of our perforated disks as

$$\phi = \frac{A_v}{\pi r^2}, \tag{10}$$

where A_v is the total area of voids, such that $\phi = 0$ corresponds to a continuous (unperforated) disk. Perforated disks were designed to have a constant porosity (void fraction), $\phi = 0.69 \pm 0.02$. This value was found to be the highest porosity to which a disk could be readily fabricated using the available laser-cutting machine. The porosity was fixed at this constant value to independently quantify how the drag ratio Ω [Eq. (2)] of porous disks depends on the geometry of the perforations. Had ϕ been left as a variable, it would have been difficult to discern variations in Ω that were due solely to changes in perforation geometry. Perforations were laser cut at the same time as the disk fabrication and comprised a hexagonal arrangement of circular voids within an uncut annulus that provided rigidity and inhibited bending during experiments. The porosity was verified postfabrication by comparing the masses of the perforated disks to those of unperforated reference disks with the same thickness.

The patterns of all perforated disks were generated by fitting a hexagonal lattice with a motif of small circles inside the annular border. Given the side length h of the unit cell associated with the lattice, the radius of all circles was $r_c = 0.45h$. Scanned images of representative disks are shown in Fig. 2. In many of the configurations shown, voids near the thin uncut band at the edge of the disk were not circular [see especially disks (vi) and (viii) in Fig. 2], so the voids had a distribution of sizes. Thus, we characterized the void sizes of a disk using an effective hole radius a instead of the radius of the circular voids. We computed a by dividing the total area of voids, $A_v = \pi r^2 \phi$, by the number of voids n to find the radius of n equally sized effective circles as

$$a = r\sqrt{\frac{\phi}{n}}. \tag{11}$$

C. Characterization of the hydrodynamic drag of the disks

Two types of experiments were performed: one using reference solid disks to confirm that our force measurements corresponded to the theoretical predictions (Sec. III A) and the other to

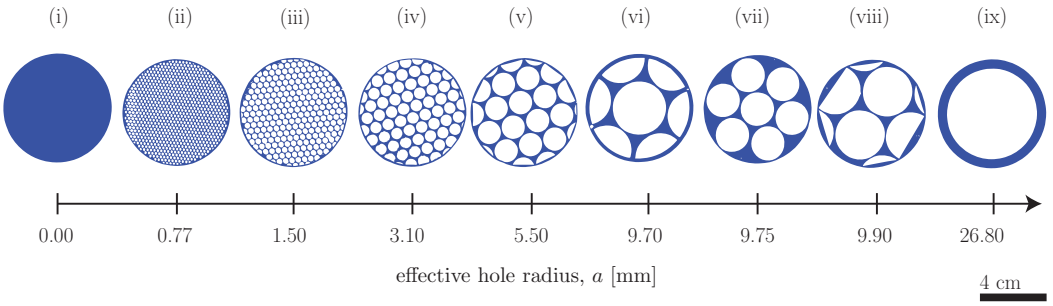

FIG. 2. Scanned images of the set of disks used in the experiments (thickness $t = 0.80 \pm 0.01$ mm). Disk (i) has no voids; disks (ii)–(ix) have constant void fractions ($\phi = 0.69 \pm 0.02$), and the size and number of voids are varied. The effective void radius a is the idealized radius calculated for n equally sized voids whose collective area is equal to the void area.

test the effect of the void size on the disks with set values of porosity (Sec. III B). For the first, unperforated disks with a constant thickness $t = 0.80 \pm 0.01$ mm but varying radii (11 values) from $12.7 \leqslant r \leqslant 52.5$ mm were used. For the second, disks with a constant porosity $\phi = 0.69 \pm 0.02$ and $r = 32.5$ mm but varying thickness t (eight values) and a varying number of voids n (eight values) were used. In addition, unperforated reference disks with $r = 32.5$ mm for each value of t were tested to normalize the results for the porous ones. Despite the slenderness of the disks, no deflection due to hydrodynamic loading was found in any of our experiments. As such, throughout, we shall regard the disks as rigid.

Each experimental run comprised the following sequence of steps: (a) measuring the oil temperature to determine the oil viscosity and avoid uncertainties due to thermal variations; (b) mounting the disks onto the UTS and ensuring levelness; (c) finding the initial depth, $z_0 = 30$ mm; (d) driving the sample through the fluid at a set speed $U = dz/dt$; and, finally, (e) returning the sample to the starting depth and removing the excess oil on the Nitinol rods accumulated due to viscous coating. The disks were driven through the oil starting at $z = 30$ mm until well before the floor of the container started to have a non-negligible effect on the force signal (at about 30 mm from the floor of the container). For statistical purposes, each characterization involved repeating steps (d) and (e) at least 12 times for different speeds, in the range $0.7 \leqslant U \leqslant 3.0$ cm/s in mineral oil or $0.01 \leqslant U \leqslant 1.1$ cm/s in silicone oil.

The raw data from each realization, for a given set of input parameters, consisted of a force signal $F(z)$, exhibiting an initial transient regime followed by a quasisteady regime (hereafter called regimes I and II). Figure 3(a) shows the raw force signal $F(z)$ as a function of the height z for a representative reference case at the following parameter set: $r = 32.5$ mm, $a = 0$ mm, $n = 0$, $t = 3.23$ mm, $\mu = 0.237$ Pa s, and $U = 3.0$ cm/s. Since we are interested exclusively in the steady-state hydrodynamic behavior of the disks, we focused our analysis only on regime II. Multiple physical mechanisms are included in the magnitude of the measured total force $F(z)$, namely, the average hydrodynamic load on the disk (which can be continuous or porous), $F_d(U)$; the hydrodynamic load on the rods that support the disk, $F_R(z, U)$; and the total buoyancy of the disk-rods system [part of which we can readily remove from our analysis by subtracting a tare to the measured force at the start of the experiments, and the other part due to the rods of which we account for with $F_R(z, U)$]. In Appendix B, we present the systematic procedure that we developed to isolate the contribution of the force on the disk $F_d(U)$ from the raw measurement $F(z)$.

Once the average hydrodynamic load on the disk, $F_d(U)$, was obtained, a final correction had to be considered to take into account the finite-size effects due to the presence of walls, as is common in confined low Re viscous flows [47]. In particular, as described above, all the experiments were performed in a cylindrical container of radius $R_p = 70$ mm, using a variety of disks with radii in the range $12.7 \leqslant r \leqslant 52.5$ mm, leading to a confinement ratio r/R_p ranging from 0.18 to 0.75,

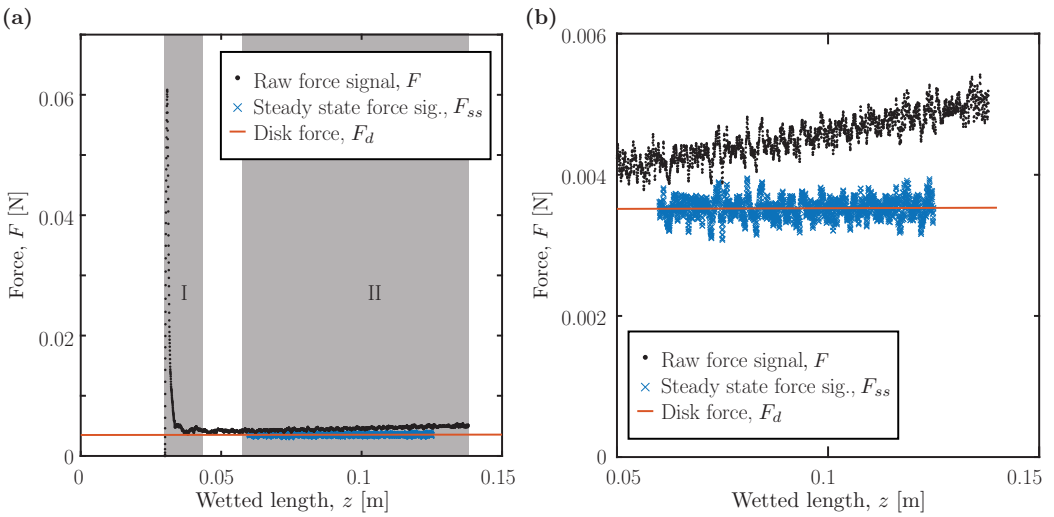

FIG. 3. The raw force signal from the load cell is plotted as a function of wetted length z, measured by the UTS (black circles). Once the transient forces—highlighted region I in (a)—have subsided, the disk experiences a steady force and the force on the rods increases: highlighted region II in (a), enlarged in (b). The steady-state disk force signal $F_{\rm ss}$ is isolated from the total force signal (see Fig. 12) and plotted as blue crosses. The horizontal red line is the average F_d of the $F_{\rm ss}$ signal. The procedure to obtain these force signals is detailed in Appendix B.

suggesting that significant changes in the hydrodynamic load are expected. Specifically, the presence of a boundary is known to increase the magnitude of the force experienced by an object moving relative to a viscous fluid under low Re number conditions, which has been studied for a variety of geometries [47]. For the specific case of an impervious disk of infinitesimal thickness moving broadside with a constant velocity along the axis of a pipe, the wall effect has been analytically predicted by Wakiya in 1957 [48] to increase by a factor α, i.e., $\alpha \geqslant 1$, with the confinement r/R_p, such that

$$F_d = \alpha F_{d,\infty}, \quad \text{where} \quad \alpha = \left[1 - 1.786\left(\frac{r}{R_p}\right) + 1.128\left(\frac{r}{R_p}\right)^3\right]^{-1}, \tag{12}$$

and where F_d and $F_{d,\infty}$ are the values of the drag forces in the presence of the container and in an unbounded viscous fluid, respectively. Wakiya computed this wall-effect factor α numerically by analyzing the viscous flow around a spheroid in the limit of zero thickness [48], as a generalization of the analysis of a sphere moving through a viscous fluid between two plates [47,49].

The geometry of our experimental system is nearly identical to that treated in Wakiya's theory, except for the finite thickness of the disks. Considering the reference impermeable disks, the relation in Eq. (12) can then be used indirectly to validate the experimental procedure described up to now, as it will be discussed in Sec. III A. To the best of our knowledge, there is no corresponding work in the literature to account for the wall effect when porous thin disks are considered; hence, in the first instance, we will assume that Wakiya's Eq. (12) remains valid for porous disks, checking *a posteriori* the compatibility of the results with those available in the literature. These arguments will be the core of our discussion in Secs. III B and III C.

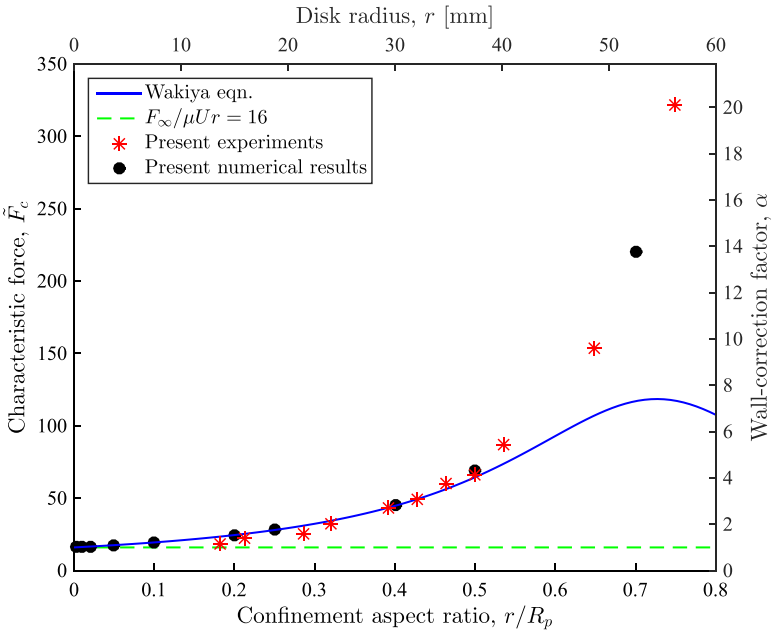

FIG. 4. Experiments were conducted with reference (unperforated) disks of varying radii to explore the wall effect. The characteristic force derived from the analytical prediction for the force on a disk by Sampson [39], shown with the green dashed line, does not account for the presence of the fluid boundary. The wall effect is accounted for in the solution given by Wakiya [48], shown with the blue solid line. Uncertainty in the radius measurements and the characteristic forces are much smaller than the size of the data points (red asterisks) and are not shown here. The results of our numerical simulations are reported with the solid black circles. [Wakiya eqn. = Eq. (12).]

III. RESULTS

In this section, the results of the experimental and numerical activities are described, starting with the reference (unperforated) disks and then turning to the perforated disks.

A. The reference unperforated disks: Validation of the experimental procedure

In Fig. 4, we present the results from a systematic set of experiments designed to validate the experimental procedure developed here to explore the effect of wall confinement, r/R_p, on the drag force for the reference disks. The results are shown in terms of normalized mean characteristic force $\tilde{F}_c$, defined as the mean of $F_d/\mu_i U r$ from all the experimental runs, each normalized by the velocity U, viscosity μ, and radius r. The subscripts $i = \{1, 2\}$ for μ_1 or μ_2 are taken from Eq. (A1) and correspond to the cases of mineral oil or silicone oil, respectively.

The normalized mean characteristic force $\tilde{F}_c$ was determined for 11 reference (unperforated) disks of radii in the range $12.6 \leqslant r \leqslant 52.5$ mm, all with the same thickness $t = 0.80$ mm, in mineral oil, using the protocol described in Sec. II C. If the presence of the boundary had no effect on the hydrodynamic loading of the disk, the normalized characteristic force of each of the disks tested would be close to Sampson's disk solution, $\tilde{F}_c = 16$ [39], within experimental error. However, as shown in Fig. 4, this is only the case for the smallest confinement ratio ($r/R_p = 0.18$). As r/R_p increases, $\tilde{F}_c$ increases by up to a factor of 20, *vis-à-vis* Sampson's solution, due to wall effects.

The results presented in Fig. 4 for disks with $r/R_p \lesssim 0.5$ (radii $r \lesssim 35.0$ mm) show excellent agreement with Wakiya's prediction, with no fitting parameters (all measurements of the relevant quantities were done independently). Moreover, when the disk radius is small ($r \lesssim 20$ mm), the

characteristic force is close to the unbound prediction ($\tilde{F}_c = 16$). These findings point to the validity of our procedure of isolating the disk force $F_d(U)$ from the total measured force $F(z, U)$ (see Appendix B) for calculating $\tilde{F}_c$. Had there been systematic errors in F_d, an offset in $\tilde{F}_c$ would have been evident in Fig. 4, which is not the case. Furthermore, if significant hydrodynamic interactions between the rods and the disks occurred, $\tilde{F}_c$ would likely not have followed Eq. (12) so closely. Finally, the agreement between Wakiya's theory and our experimental results provides evidence for the following observations: (i) given that the theory was derived in the Stokes limit, classifying the experimental conditions as low Re numbers is acceptable, even though the Reynolds numbers based on the disk diameter are $\mathrm{Re} = O(1\text{–}10)$ and (ii) the thickness of the disks does not seem to have a dominant effect, given that the theory assumes infinitesimally thin disks.

For $r/R_p \gtrsim 0.5$, Eq. (12) underpredicts the magnitude of the force. This is likely due to the fact that in Wakiya's solution, only two reflections are considered in the underlying method of images. Considering additional reflections would have likely performed better at higher values of the confinement [47]. Furthermore, the theory is based on an expansion procedure, so for large values of r/R_p, it is no longer expected to be appropriate. The solid black circles represent the numerical solution for Stokes flow, which will be discussed in detail in Sec. III C.

B. Experimental results: The perforated disks

Having validated the experimental procedure in the previous section, we turn to present the results for the case of perforated disks. We give particular attention to the drag ratio Ω, defined as the experimentally measured drag force on the permeable disk, normalized with the drag on an impervious reference disk of corresponding thickness [Eq. (2)].

We seek to characterize the dependence of Ω on, first, the thickness of the disks, t, and, then, on the effective radius of the voids, a, defined in Eq. (11). We recall that throughout the experiments, the porosity was kept at the constant value of $\phi = 0.69 \pm 0.02$ [see Eq. (10)] and that the wall effect has been taken into account, at this stage of the discussion, considering the correction factors derived from the Wakiya results [Eq. (12)] available for the case of the Stokes flow past a confined impervious disk (see Sec. II C).

The experimental results are reported in Fig. 5 for disks with different values of thickness t (in the range $0.40 \leqslant t \leqslant 3.23$ mm) and various effective void radii a (in the range $1.7 \leqslant a \leqslant 26.6$ mm). In order to highlight the dependence of Ω on the two characteristic lengths t and a, the data are presented as a function of the thickness t for fixed values of a [Fig. 5(a)] and, vice versa, showing Ω as function of a for fixed values of t [Fig. 5(b)].

The experimental data show that within the experimental uncertainties, the drag ratio remains approximately constant with thickness [Fig. 5(a)], whereas the effective void radius a has a marked effect on Ω [Fig. 5(b)]. The fact that Ω is weakly dependent on t is surprising given that thicker disks have larger "through-thickness" surfaces on which shear viscous forces can act, when compared to a continuous ($\phi = 0$) reference disk. Indeed, such an argument is made by Jensen *et al.* in [50] in the context of solving for the flow rate given a pressure drop across microfilters. Adapted to the context of this paper, the findings from Jensen *et al.* are that

$$\Delta P = \left[\frac{3\mu}{a^3}(1 - A) - 2.3\left(\frac{a}{L}\right)^3\right]Q, \quad A = \frac{8t}{3\pi a}, \tag{13}$$

where A is, up to a scaling factor, the ratio between the membrane width t and the aperture radius a, L is the average center-to-center distance between pores, and Q is the volumetric flow rate through the microfilter. Within the brackets, the first and second terms account for the effects of aperture and Poiseuille flows, respectively, and the third term accounts for pore-pore hydrodynamic coupling. Consider the case of $a = 1.7$ mm in Fig. 5(a). In this subset of the data, the pore-pore hydrodynamic coupling is constant and $0.25 \lessapprox A \lessapprox 1$. The Poiseuille behavior of the pores, then, should be four times as important for the thickest disk as it is for the thinnest disk. Yet, as is shown in Fig. 5(a), this is not reflected in the drag ratio. Presumably, this could be because of the unconfined nature of

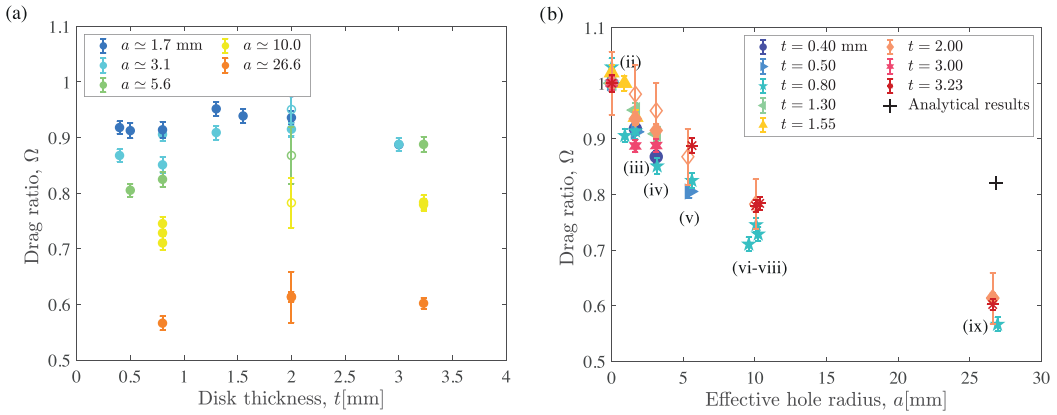

FIG. 5. (a) The drag ratio is plotted as a function of thickness for different effective void radii (see legend). Open and closed symbols correspond to experiments conducted in the lower Reynolds number [Re $= O(10^{-4}$–$10^{-3})$] and the higher Reynolds number [Re $= O(1$–$10)$] conditions, respectively. (b) The drag ratio Ω decreases as the effective void radius a increases for disks with radius $r = 3.25$ cm (fixed porosity $\phi = 0.69 \pm 0.02$). The roman numerals correspond to the scanned disks in Fig. 2. Open and closed symbols correspond to experiments conducted in the lower Reynolds number [Re $= O(10^{-4}$–$10^{-3})$] and the higher Reynolds number [Re $= O(1$–$10)$] conditions, respectively. The analytical result (+ symbol) for the annular disk is obtained from Eq. (7). In both (a) and (b), the error bars reflect uncertainty in Ω which propagates due to uncertainty in $\tilde{F}_c$. When the wall effects for porous disks are appropriately taken into account towards the end of the paper, the drag ratio as a function of the void size is corrected.

the disk; fluid is permitted to travel not only within the porous structure, but also around it. Given an effective void radius, the corresponding experimental drag ratios for different disk thicknesses, t, are nearly constant, with typical deviations from the mean value of less than 6%. Lastly, we also note that referring to Eq. (9), the negligible impact of the thickness on Ω suggests a possible linear scaling of the permeability k with t, when a homogenized porous media is considered as an appropriate model for the behavior of the flow past perforated disks. This point will be discussed in more detail in Sec. IV, where we will also propose a possible scaling of the permeability versus void size.

Next, we discuss the dependence of hydrodynamic load on the effective void size a. It is important to recall that the void fraction was kept constant throughout the experiments at $\phi = 0.69 \pm 0.02$, while varying numbers of voids and their dimensions. From the results in Fig. 5(b), we find that the drag ratio decays monotonically with increasing void size, from $\Omega = 1$ at $a = 0$ (the unperforated reference disks), down to $\Omega \approx 0.6$ for perforated disks with an effective void size of $a = 26.6$ mm [the annular disks (ix)]. Therefore, the hydrodynamic drag decreases when permeability increases. However, the resulting reduction of the drag ratio is too large as in the case of largest permeability, which is an annular disk, the predicted drag ratio is smaller than the analytical prediction already mentioned in Sec. I. In particular, recalling Eq. (7), we can infer that the analytical prediction of the drag on the annular disks (ix) is $\Omega \approx 0.82$, whereas with the results reported in Fig. 5(b), for the same configurations, we find $\Omega \approx 0.6$. The data presented in Fig. 5 use the wall-effect correction factor α, analytically predicted by the Wakiya's approximation [Eq. (12)], for the Stokes flow past an impervious thin disk. Therefore, we could ascribe these discrepancies to unrealistic wall-correction factors. Here we note that the dependency of Ω on a could be in part due to pore-pore hydrodynamic interactions [50]. Instead of quantifying the effect of these couplings, we encapsulate them within the permeability, which we will solve for in Sec. IV.

As will become clear in the next section, the use of wall-effect factors (originally evaluated for solid impervious obstacles) to porous disks leads to an underestimation of the hydrodynamic forces.

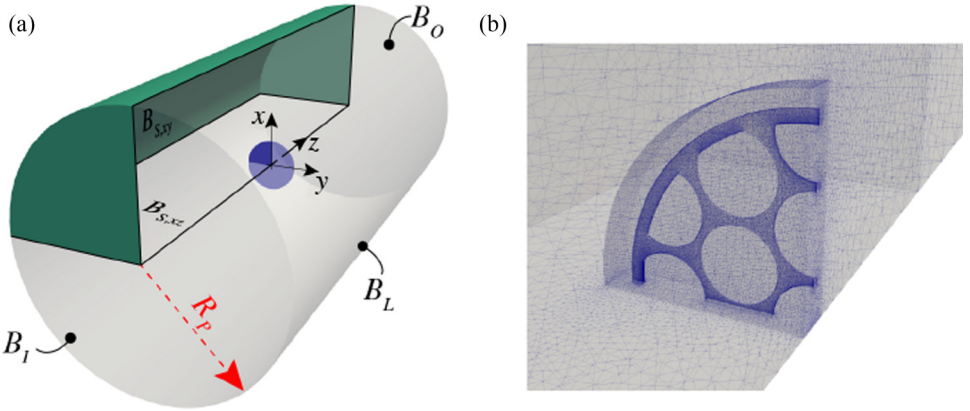

FIG. 6. (a) Sketch of the numerical flow configuration (not to scale); (b) representative detail of the mesh used to simulate the Stokes flow past the disk (v).

This means that wall effects for permeable disks are different from those for impervious disks. Thus, in order to have an estimation of the wall-effect for the permeable disks, numerical simulations of the Stokes flow past confined perforated disks have been carried out, which we address next.

C. Evaluation of the wall effect for porous disks

We have seen in the previous section that for permeable disks, the effect of the wall confinement must be studied for each specific case. Indeed, the effect of the walls on the solution of the flow through permeable obstacles is difficult to predict, and it differs from what we have discussed in Sec. II for impervious disks. Thus, to correct the experimental results reported in Fig. 5, we shall proceed by numerically evaluating the appropriate wall-correction factors by simulating the three-dimensional flow around and through perforated disks (i)–(ix) in a confined domain.

As sketched in Fig. 6, the flow is described in a Cartesian coordinate system that is fixed with the disks, with the x direction aligned with the incoming relative flow velocity. When the dynamics of a viscous fluid at low Re numbers are considered, the flow behavior is well described by the incompressible Stokes equations, already reported in Eq. (3). This system is then completed by the following boundary conditions: uniform velocity is imposed at the inlet boundary $\mathcal{B}_I$ and on the lateral boundary $\mathcal{B}_L$, i.e., $\boldsymbol{u} = U_\infty \boldsymbol{e_x}$, the homogeneous Dirichlet condition is considered on disk $\mathcal{B}_D$, i.e., $\boldsymbol{u} = \boldsymbol{0}$, and the no-stress condition is then applied to the outlet boundary $\mathcal{B}_O$. In order to evaluate the wall effect for different levels of confinement ratio, the radius R_P is varied, such that $0.01 \leqslant r/R_P \leqslant 0.6$.

The system of Eq. (3) was discretized in space using P2-P1 Taylor-Hood finite elements for the velocity and for the pressure, respectively. The physical domains were discretized using unstructured grids generated with the open-source code GMSH [51] and then imported in the finite-element library FreeFem++ [52], where the discretized version of Eq. (3) was solved. Three internal subregions were created to control the mesh density, here specified by the vertex densities imposed on the corresponding edges. The presence of subdomains is essential to have a good refinement of the meshes in the region close to the perforated disks, especially when cases with small void radii are considered. In Fig. 6(b), we present an example of the discretization for the disk (v). Considering the double symmetry of the Stokes solutions, only a quarter of the domain was considered; the corresponding symmetry conditions were imposed at the two corresponding lateral boundaries, i.e., $u_z = 0$ on $\Omega_{S,xy}$ and $u_y = 0$ on $\Omega_{S,xz}$. The typical grid size consisted of approximately 4.5×10^5 elements, considering at least three elements in the disk thickness, for a total number of degrees of freedom of about 2×10^6.

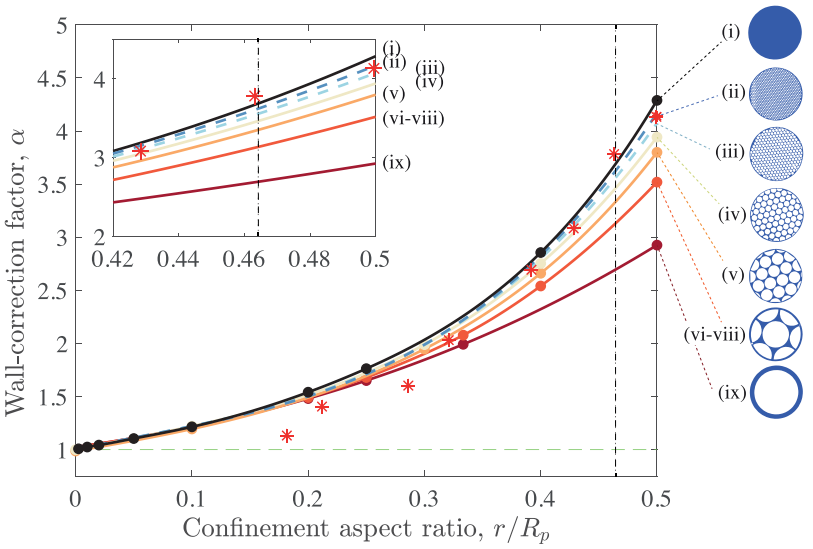

FIG. 7. The colored solid lines represent the wall-correction factors for different confinement ratios, here numerically evaluated for the disks considered in the experiments, from the case of the solid disk (i) to the annular disk (ix). The dashed green line is the characteristic force derived from the analytical prediction for the force on a disk by Sampson [39]. The vertical dashed black line corresponds to the confinement ratio used during the experiments, i.e., $\alpha(r/R_p = 0.4643)$. The red asterisks are the experimental values obtained for the reference disks, as already reported in Fig. 4.

The numerical procedure and spatial discretization were validated considering the case of the unperforated reference disk, both for the case with unbounded domain (here using $r/R_N = 400$) and for the confined configurations. Our numerical results (black circles in Fig. 4) show excellent agreement both with the analytical formula by Wakiya [Eq. (12)] and with the experimental results reported in Sec. III A. The same numerical results are reported again in Fig. 7—the continuous disk corresponds to the disk (i)—together with the numerical results for the permeable disks considered during the experiments, i.e., disks from (ii) to (ix). In particular, these values have been evaluated from the numerical simulations for the disks from (iv) to (ix), while, for the disks (ii) and (iii), the correction factors have been linearly extrapolated from the others [Fig. 8(a)] due to the demanding computational resources that the spatial discretization of these last two configurations would have involved (dashed light-blue lines). As shown in Fig. 7, for consider perforated disks, the wall-correction factor decreases as the permeability of the disk increases, namely, from disk (ii) to disk (ix). We can also see that for low confinement ratios, $r/R_N \leqslant 0.2$, no significant variations of α have been found among the different configurations investigated and the analytical result of Eq. (12) is therefore valid. On the contrary, the effect of the walls in the case of permeable disks is found to be more complex when higher confinement ratios are considered, i.e., $r/R_N > 0.2$, leading to wall-correction factors that depend on the permeability of the disk.

Having evaluated the wall-correction factors for the specific permeable disks considered in the experiments, we can now correct the experimental results using the values of α corresponding to the specific confinement ratio used in the experiments, namely, $r/R_P = 0.464$. These values of α are summarized in Fig. 8(a). The corrected experimental data are reported in Fig. 8(b) where, similarly to Fig. 5, we present the results in terms of Ω as a function of the void radii a for various thicknesses t. As a first comment, we can clearly see that while the preliminary drag ratio Ω ranged from 0.6 to 1, the variability of the adjusted drag ratio is reduced, ranging from 0.79 to 1.

There are significant modifications in the reprocessed data [Fig. 8(b)] that take into account the numerically computed wall corrections when compared to the previous data [Fig. 5(b)] that

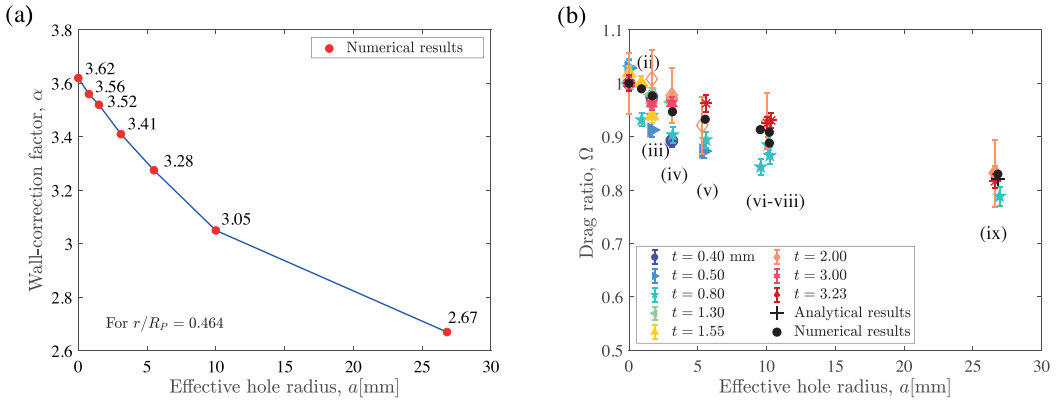

FIG. 8. (a) Wall-correction factors for the perforated disks at the experimental confinement ratio $\alpha(r/R_p = 0.464)$ as function of the void radii. The solid blue line represents the linear interpolation between the numerical correction factors. (b) Drag ratio Ω as a function of the effective void radius a, taking into account the wall effects for porous disks obtained from the numerical simulations.

was initially analyzed using Wakiya's correction [Eq. (12)]. It is evident that accounting for the confinement using appropriate wall-correction factors, the drag ratio of all the realizations is increased. In particular, the experimental values for the cases of the annular disks (ix) are now clustered around the analytical result in Eq. (7) for the corresponding inner-to-outer radius ratio [reported as a black cross in Fig. 8(b)]. The drag ratios for the other perforated cases, i.e., disks from (ii) to (viii), are higher and mostly in the range $0.85 \leqslant \Omega \leqslant 1$. These results are reasonable given that their permeabilities are higher than that of the annular disk. Finally, as a consistency check, the values of the drag ratio computed numerically for the disks from (iv) to (ix) are also reported in Fig. 8(b), showing good agreement with the experimental data. Figure 8(b) is the main finding of the paper, which we further rationalize in the next section.

IV. INTERPRETATION OF THE DRAG RATIO RESULTS WITHIN A PERMEABILITY FRAMEWORK

In this section, we interpret the above experimental results of the hydrodynamic drag ratio for disks of different layouts of voids within the framework of Darcy flow proposed by Vainshtein [22]. As is the crux of many problems involving flow through porous media [37], the permeability k of the disks must be determined to invoke Darcy's Law in Eq. (8). We address this by first proposing two possible scalings for k that depend on the dimensions of the voids (t and a) and rely on different models for the flow through them. Both of these scaling arguments involve considering the flow through the channels formed by the voids; the first uses a Poiseuille flow argument and the second employs an aperture flow argument. Each of these scalings is then tested and evaluated against our own experimental data, toward empirically identifying the most appropriate choice.

In order to determine the permeabilities k of our disks, we develop a scaling argument which relates the pressure drop through a single void to the pressure drop across the disk associated with Darcy flow. All voids are treated equally, meaning that the specific location of each void on the disk has no impact on the flow through it. Furthermore, each void has radius a and the hydrodynamic interactions between voids are assumed to be negligible. This analysis serves as a leading-order estimate. A more detailed description that also takes into account the hydrodynamic interaction of the voids is presented in Ref. [50].

In more detail, the flow through each of the voids is assumed to be classifiable into one of two flow models: for Poiseuille flow [47] and for aperture (orifice) flow [39,47]; referred to by the subscripts $j = \{1, 2\}$, respectively. We note that a third model, with a linear combination of these

flows (proposed by Weissberg [53], confirmed by Dagan [54], and used by Jensen [50]) could also have been possible, but we do not explore it here since we shall demonstrate sufficiently good agreement of aperture flow with our results. Consequently, the corresponding changes in pressure can be expressed as follows:

$$\Delta P_1 = \frac{8\mu t}{\pi a^4} q, \tag{14a}$$

$$\Delta P_2 = \frac{3\mu}{a^3} q, \tag{14b}$$

where, in both cases, q is the volumetric flow rate of a fluid with viscosity μ, through a single hole of size a. This pressure drop ΔP_j occurs over a distance t in the Poiseuille model ($j = 1$), and over a distance comparable with the dimension of the orifice in the orifice flow model ($j = 2$). It is important to note that the pressure becomes uniform when the distance from the orifice becomes larger than a few a. This is a consequence of constant pressure radial sink (or source) flow prevailing away from the orifice. Note also that Eq. (13) neglects any collective effects. In the orifice flow, those have been analyzed in Ref. [50] [also Eq. (13) in this paper] and in Ref. [47]. They have found that the pressure jump is reduced by collective effects, depending on the distance between two hole centers L and the lattice on which the holes are located. In the worst-case scenario $L = 2a$, $\Delta P/Q$ is reduced by $2.3/8 = 28\%$, assuming a hexagonal lattice. In order to determine the permeability k, we relate each of the above pressure-drop models to that associated with the Darcy's equation:

$$\Delta P_D = -\frac{\mu t}{k} \frac{Q}{\mathcal{A}}, \tag{15}$$

where $Q = nq$ is the total volumetric flow rate across all the holes, over a distance t, and the cross-sectional area is assumed to scale with the total projected area, $\mathcal{A} \sim r^2 = na^2/\phi$. Away from this porous disk, the flow is governed by the Stokes equation and the pressure becomes again constant, sufficiently far from the disk. We therefore equate the Darcy pressure drop with the pressure drop associated with each of the j flow model yields,

$$\Delta P_j \sim \Delta P_D. \tag{16}$$

Finally, solving for the permeability and dropping the porosity term since all experiments were conducted with a constant $\phi = 0.69 \pm 0.02$, we find that the scalings for the permeability for the two cases are, respectively,

$$k_1 \sim a^2, \tag{17a}$$

$$k_2 \sim at. \tag{17b}$$

Next, we shall evaluate which of the two scalings above for k_j is most appropriate by testing them against the experimental data.

To interpret our experimental results in the framework of Darcy flow, we must first determine the actual form of the permeability k. We do so by comparing each of the two possible scalings presented in Eqs. (17a) and (17b) to Vainshtein's solution [22] for flow through and around a porous disk, whose permeability is denoted by k_V. Recalling Eq. (9), Vainshtein's solution can be rewritten as a function of the experimentally measurable physical quantities,

$$k_V = \pi rt \frac{1 - \Omega}{\Omega}. \tag{18}$$

In Fig. 9(a), we plot k_V, computed through the experimental data, versus k_1, determined from Eq. (17a). In Fig. 9(b), we plot the same k_V as a function of k_2, from Eq. (17b). Comparing both plots suggests that the second alternative, coming from the orifice flow model, that is, $k_V \sim k_2 \sim at$, is a more appropriate description of the data given the more effective collapse of the data. The prefactor $c = k_2/(at)$ was determined to be $c = 0.97 \pm 0.02$ from a linear least-squares fit.

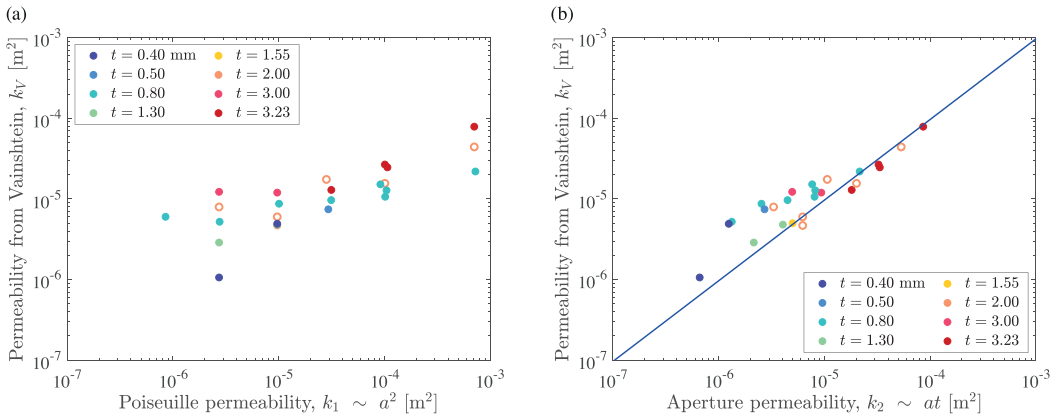

FIG. 9. Experimentally determined permeability k_V computed through Eq. (18) vs (a) $k_1 \sim a^2$ and (b) $k_2 \sim at$. The solid symbols correspond to experiments done at $\mathrm{Re} = O(1\text{–}10)$, for the mineral oil, and open symbols correspond to experiments conducted at $\mathrm{Re} = O(10^{-4}\text{–}10^{-3})$, for the silicone oil. Error bars in the vertical direction represent the experimental uncertainty in Ω propagating from the the rod force. Error bars are smaller than the solid data points.

As the final step of our investigation, we revisit the original formulation of the solution of Darcy flow through the disk. Recalling the definition of the Brinkman parameter, $\beta = \sqrt{rt/k}$, from Sec. I, making usage of Eq. (9), and taking $k = k_2 = cat$ with $c = 0.97 \pm 0.02$ determined above, we can now plot the experimentally measured drag ratio Ω versus β, which is shown in Fig. 10. We recall that the Brinkman parameter β characterizes the permeability of the disk relative to its size, which we took to be described by its radius r and its thickness t. When $\beta \lesssim 2$, we find that $\Omega \ll 1$, signifying that the perforations (voids) are important in reducing the experienced hydrodynamic drag. For $\beta \gtrsim 2$, the voids have no apparent effect on the hydrodynamic load of the disks and $\Omega \approx 1$. Note that Eq. (9) is expected to be valid across all values of β. However, the smallest possible value

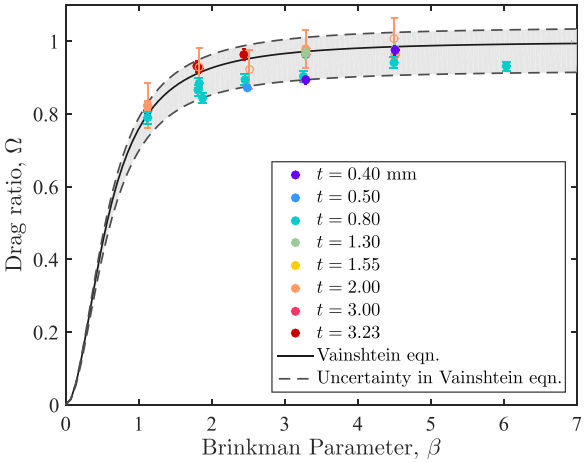

FIG. 10. Drag ratio Ω as a function of the Brinkman parameter β. The solid symbols correspond to experiments conducted at $\mathrm{Re} = O(1\text{–}10)$ (with the mineral oil) and open symbols correspond to experiments conducted at $\mathrm{Re} = O(10^{-4}\text{–}10^{-3})$ (with the silicone oil). Error bars of the data points correspond to uncertainty in the rod force. Uncertainty in the prediction (shown shaded in gray) is due to uncertainty in the prediction of k. [Vainshtein eqn. = Eq. (9).]

of this Brinkman parameter in our experiments is $\beta = 1.124$, which corresponds to the case of the disk being perforated with just one hole, $n = 1$, with the porosity $\phi = 0.69 \pm 0.02$ [this case corresponds to the disk (ix) in Fig. 2]. The solid line in Fig. 10 corresponds to the Vainshtein prediction given in Eq. (9) using a fitted value of $k = cat$, with $c = 0.97 \pm 0.02$. The shaded region corresponds to the drag ratio calculated using Eq. (9) within the 95% confidence interval obtained from the fitted k. Excellent agreement is found between our experimental data and Vainshtein's description.

V. DISCUSSION AND CONCLUSION

We have shown that the hydrodynamic loading of perforated disks at low Reynolds number conditions is strongly dictated by the effective size of the voids, while keeping the porosity fixed. Through displacement controlled experiments, we have focused our investigation on the drag ratio Ω, comparing the drag that a porous disk experiences with respect to a continuous (unperforated and impermeable) reference disk. In particular, Ω was found to depend on the effective void radius, but not on the thickness of the disks. When the effective radius of the voids is small, the drag experienced by the perforated disks is close to that experienced by disks without perforations. On the other hand, a disk with the same porosity but with a larger effective void radius exhibited a significant reduction in drag, depending on the selected porosity. We have rationalized our findings by implementing a scaling argument that connected the geometric parameters of the voids to the permeability of the disks. The efficacy of our experimentally guided analysis was tested against the permeability from Vainshtein's solution [22], and good agreement was observed.

An important finding that was crucial for our study is the evaluation of the wall effects for porous structures. Our experimental results, supported and enriched by the numerical simulations, show that for large confinement, the wall effects deviate from Wakiya's correction, which was indeed derived for impermeable disks. In general, we show that wall effects become increasingly important as permeability decreases, that is, as holes become smaller and more numerous.

We close by providing a speculation on a potential application of our results. Our findings could, for example, be harnessed to reduce the weight of porous devices such as microrobots, whose power consumption triples as their weight doubles [49]. While most of the weight budget (approximately 70%) of such systems is dedicated to the electronics, motors, actuators, and battery, the remaining 30% is taken by the air frame [49]. Reductions in the weight of the air frame by introducing porosity could enable further reductions in the battery size necessary for flight, without significantly comprising the fluid loading.

APPENDIX A: DETERMINATION OF THE VISCOSITY OF THE FLUIDS USED

Two oils were used: a mineral oil (Crystal Plus Food Grade 500FG, STE Oil Company, Inc.) with a dynamic viscosity on the order of 10^{-1} Pa s and a density of $\rho_1 = 868$ kg/m^3; and a silicone oil (DMS-T51, Gelest) with a dynamic viscosity on the order of 10^2 Pa s and a density of $\rho_2 = 977$ kg/m^3. The Reynolds number for all experiments was defined as $\mathrm{Re} = \rho U 2r/\mu$, taking the diameter of the disk, $2r$, as the characteristic length scale. The dynamic viscosity of these two oils was determined as functions of temperature T, using a rheometer (AR-G2, TA Instruments) with a 40 mm steel cone with an angle of 2°. The shear rate was fixed at $\dot{\gamma} = 2.856$ s^{-1}, which was estimated to be comparable to the shear rates encountered in the experiments, and the oil temperature T was decreased from $T = 28$ °C to $T = 16$ °C, over the course of 20 minutes.

In Fig. 11, we plot the dynamic viscosity as a function of temperature, for both of the oils (green squares for the silicone oil and red crosses for the mineral oil). The experimental data is found to be well fitted (dashed and solid lines, respectively, in Fig. 11) by an Arrhenius description [55]:

$$\mu_i = A_i e^{B_i/(T+273.15)}, \tag{A1}$$

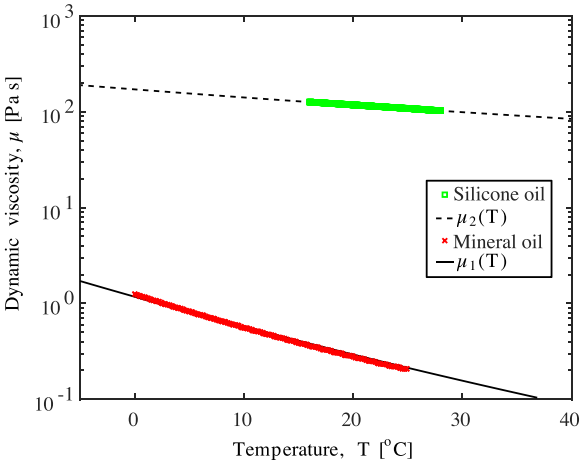

FIG. 11. Temperature dependence of the dynamic viscosity of both fluids used: silicone oil and mineral oil (see legend). The dashed and solid lines correspond to fits to Eq. (A1) for the two oils, respectively.

where μ is given in units of Pa s, T in °C, and the subscripts $i = 1, 2$ correspond to the mineral and silicone oils, respectively. The fitting coefficients were determined to be $A_1 = (1.46 \pm 0.39) \times 10^{-9}$ Pa s and $B_1 = 5604 \pm 73$ °C for the mineral oil and $A_2 = 0.688 \pm 0.005$ Pa s and $B_2 = 1508 \pm 3$ °C for the silicone oil. The temperature of the room where the experiments were performed could vary on a day-to-day timescale in the range $18 \leqslant T \leqslant 24$ °C. To circumnavigate this practical but inevitable issue in our laboratory, T was measured before each experimental test and used to determine the corresponding value of the viscosity of the oil through Eq. (A1). Both fluids were found to behave as Newtonian fluids for $\dot{\gamma}_1 < 10^2$ s^{-1} [56] and $\dot{\gamma}_2 < 10^4$ s^{-1} [57], which are shear rate values much larger than those encountered in our experiments, so we assume that the behavior of each in our experiments is Newtonian.

APPENDIX B: CALIBRATION OF THE FORCE ON THE SUPPORTING RODS TO DETERMINE THE LOAD ON THE DISK

In the steady-state regime [regime II in Fig. 3(a)], the component of the hydrodynamic load associated with the disk, $F_{ss}(U)$, is expected to be constant, while the component associated with the rods, $F_R(z, U)$, grows with increasing z (due to an increasing wetted length). The steady-state force on the disk can therefore be isolated from the total load signal as

$$F_{ss}(U) = F(z, U) - F_R(z, U), \tag{B1}$$

whose average we define as the characteristic force exerted on the disk,

$$F_d(U) = \langle F_{ss}(U) \rangle. \tag{B2}$$

The component of the loading attributed to the rods, $F_R(z, U)$, results from a combination of hydrodynamic loading, buoyancy, and air entrainment near the free surface. Next, we focus on calibrating $F_R(z, U)$, so that $F_d(U)$ can be obtained through Eq. (B1). Separate experiments were conducted to determine $F_R(z, U)$ for the mineral and silicone oils. In these calibration experiments, we followed the experimental protocol detailed in Sec. II C. However, in contrast to all the other experiments described in this paper which use two rods to support the disks, we used a varying numbers of rods attached to calibration disks to ensure that each rod introduces the same force. To confirm this, we also conducted experiments with varying numbers of rods but no calibration disk at all. First, we assume that each of the n_r supporting rods experiences the same force as a function of speed, so $F_R(z, U) = F_r(z, U)\, n_r$, which implies that the rod-rod and rod-disk cross interactions are

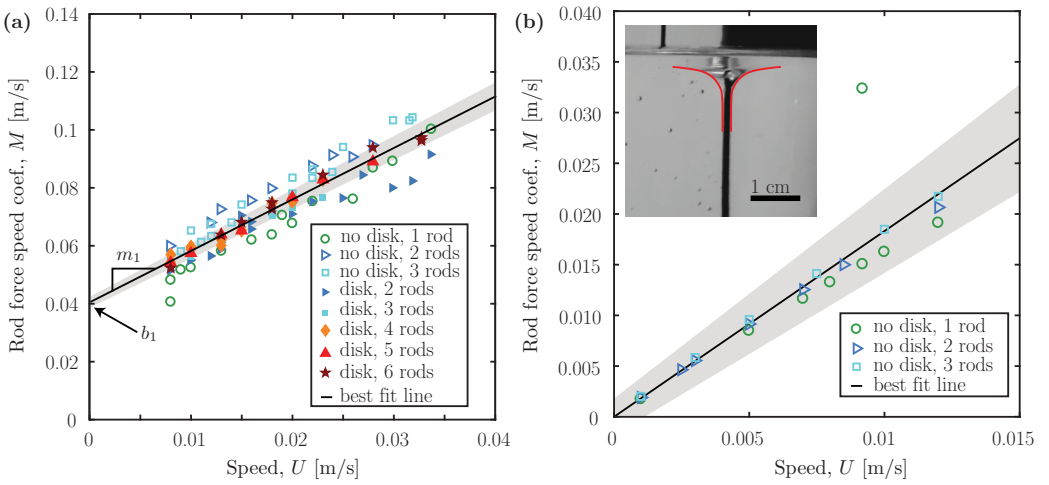

FIG. 12. The rod force-speed coefficient M, defined in Eq. (B3), is plotted as a function of the speed U for (a) the mineral oil and (b) the silicone oil. In both plots, the solid line is the fitted $M(U)$ and the gray region represents the 68% confidence interval in both fitted parameters. The outlier data point in (b) was preserved because we could not recall any abnormalities regarding the particular experiment from which it came. The inset in (b) shows the air entrainment that occurred at the free surface in experiments using the silicone oil. Error bars corresponding to variation in the steady-state force signal F_{ss} and the disk speed U are smaller than the data points and are not shown.

negligible. Furthermore, we also assume that first, the rods only contribute to the slope of $F(z, U)$ with increasing z, and, second, the slope of $F(z, U)$ versus z is caused entirely by the rods.

The calibration of the effect of the rods in the mineral oil was conducted first. We carried out two sets of experiments, as described above in Sec. II C. In the first, we ran the experiments using the same disk ($r = 3.75$ cm, $a = 2.5$ cm, $t = 0.80$ mm) supported by $n_r = 2, 3, 4, 5$, or 6 rods such that the total force was given by $F(z, U) = F_d(U) + n_r F_r(z, U)$. The F_d component of the force was assumed to remain constant with z in the steady-state regime, so any change of the force signal with displacement was attributed to the rods. In the second, we ran experiments *without* a disk using only one, two, or three rods so that $F(z, U) = n_r F_r(z, U)$. Given the practical challenges of working with the more viscous silicone oil (namely, cleanliness) and the efficacy of the mineral oil calibration, the calibration for the rod effect in the silicone oil involved only the first experiment.

As above, the subscript i denotes the selected oil ($i = 1$ for mineral oil and $i = 2$ for silicone oil). The slope m_i of the best linear fit to regime II of the $F(z, U)$ data in Fig. 3(a) was divided by both the number of rods, n_r, and the fluid viscosity, given by Eq. (A1), to obtain $M_i = m_i/(\mu_i n_r)$ m/s, which we shall refer to as the *force-speed coefficient of the rod*. The reason for treating the data in this apparently cumbersome way is so as to scale out changes of viscosity due to temperature variations (for experiments performed in different days), which can be taken into account using Eq. (A1). In Fig. 12, we plot M_i as a function of U, for a variety of different disk and rod combinations, finding a linear relation of the form

$$M_i(U) = m_i U + b_i, \tag{B3}$$

where the coefficients m_i and b_i were determined using a linear least-squares fit. The collapse of the data provides evidence for the validity of the assumption that the rod-rod and the rod-disk interactions are negligible. For the mineral oil, $m_1 = 1.77 \pm 0.07$ and $b_1 = 0.040 \pm 0.002$, where the uncertainties correspond to the 68% confidence intervals of the fit. This uncertainty reflects the minimum resolution of our force measurements and is the basis for the uncertainty which propagates throughout the remainder of the analysis. For the silicone oil, we obtained $m_2 = 1.8 \pm 0.2$ and

$b_2 = 0.000 \pm 0.002$. We suspect that the difference between the values of the offset b for the two oils is due to the fact that air entrainment at the free surface was significantly pronounced for the silicone oil [see photograph in Fig. 12(b), inset], but less so for the mineral oil. Moreover, buoyancy and viscous loading was also different for the two oils.

The calibrated rod force is then subtracted from the total force signal, through Eq. (B1), with $F_R(z, U) = n_r F_r(z, U) = n_r \mu_i M_i(U) z$, to isolate the steady-state force signal, $F_{ss}(U)$, and, hence, the average disk force $F_d(U)$. An example of the outcome of this procedure is presented in Fig. 3(b); the rod force is subtracted from the raw force signal (black circles) to give the steady force (blue crosses) to yield the average disk force (horizontal red line).

[1] M. A. R. Koehl, J. R. Koseff, J. P. Crimaldi, M. G. McCay, T. Cooper, M. B. Wiley, and P. A. Moore, Lobster sniffing: Antennule design and hydrodynamic filtering of information in an odor plume, Science **294**, 1948 (2001).

[2] M. A. R. Koehl, Biomechanics of microscopic appendages: Functional shifts caused by changes in speed, J. Biomech. **37**, 789 (2004).

[3] C. Geierman and R. Emlet, Feeding behavior, cirral fan anatomy, Reynolds numbers, and leakiness of balanus glandula, from post-metamorphic juvenile to the adult, J. Expt. Mar. Biol. Ecol. **379**, 68 (2009).

[4] D. M. Karl, G. A. Knauer, and J. H. Martin, Downward flux of particulate organic matter in the ocean: A particle decomposition paradox, Nature (London) **332**, 438 (1988).

[5] M. Gehlen, L. Bopp, N. Emprin, O. Aumont, C. Heinze, and O. Ragueneau, Reconciling surface ocean productivity, export fluxes and sediment composition in a global biogeochemical ocean model, Biogeosciences **3**, 521 (2006).

[6] I. Kriest and A. Oschlies, On the treatment of particulate organic matter sinking in large-scale models of marine biogeochemical cycles, Biogeosciences **5**, 55 (2008).

[7] C. P. Johnson, X. Li, and B. E. Logan, Settling velocities of fractal aggregates, Environ. Sci. Technol. **30**, 1911 (1996).

[8] G. C. Trager, J.-S. Hwang, and J. R. Strickler, Barnacle suspension-feeding in variable flow, Marine Biol. **105**, 117 (1990).

[9] C. Cummins, M. Seale, A. Macente, D. Certini, E. Mastropaolo, I. M. Viola, and N. Nakayama, A separated vortex ring underlies the flight of the dandelion, Nature (London) **562**, 414 (2018).

[10] D. F. Lawler, Removing particles in water and wastewater, Environ. Sci. Technol. **20**, 856 (1986).

[11] S. K. Jones, Y. J. J. Yun, T. L. Hedrick, B. E. Griffith, and L. A. Miller, Bristles reduce the force required to fling wings apart in the smallest insects, J. Expt. Biol. **219**, 3759 (2016).

[12] F. M. Burrows, *Seed Dispersal* (Academic, San Diego, 1986), pp. 1–47.

[13] J. Ackerman, Submarine pollination in the marine angiosperm zostera marina (zosteraceae). I. The influence of floral morphology on fluid flow, Am. J. Bot. **84**, 1099 (1997).

[14] M. Kajikawa, Measurement of falling velocity of individual snow crystals, J. Meteorol. Soc. Jpn. Ser. II **50**, 577 (1972).

[15] R. A. Houze, Jr., *Cloud Dynamics*, Vol. 104 (Academic Press, San Diego, California, 1993).

[16] A. J. Heymsfield and J. Iaquinta, Cirrus crystal terminal velocities, J. Atmos. Sci. **57**, 916 (2000).

[17] P. Vainshtein, M. Shapiro, and C. Gutfinger, Mobility of permeable aggregates: Effects of shape and porosity, J. Aerosol. Sci. **35**, 383 (2004).

[18] G. Neale, N. Epstein, and W. Nader, Creeping flow relative to permeable spheres, Chem. Eng. Sci. **28**, 1865 (1973).

[19] J. J. L. Higdon and M. Kojima, On the calculation of Stokes' flow past porous particles, Int. J. Multiphase Flow **7**, 719 (1981).

[20] G. Ooms, P. F. Mijnlieff, and H. L. Beckers, Frictional force exerted by a flowing fluid on a permeable particle, with particular reference to polymer coils, J. Chem. Phys. **53**, 4123 (1970).

[21] D. N. Sutherland and C. T. Tan, Sedimentation of a porous sphere, Chem. Eng. Sci. **25**, 1948 (1970).
[22] P. Vainshtein, M. Shapiro, and C. Gutfinger, Creeping flow past and within a permeable spheroid, Int. J. Multiphase Flow **28**, 1945 (2002).
[23] H. C. Brinkman, A calculation of the viscous force exerted by a flowing fluid on a dense swarm of particles, Flow, Turbulence and Combustion **1**, 27 (1949).
[24] R. M. Wu and D. J. Lee, Highly porous sphere moving through centerline of circular tube filled with Newtonian fluid, Chem. Eng. Sci. **54**, 5717 (1999).
[25] A. K. Jain and S. Basu, Flow past a porous permeable sphere: Hydrodynamics and heat-transfer studies, Ind. Eng. Chem. Res. **51**, 2170 (2011).
[26] K. Matsumoto and A. Suganuma, Settling velocity of a permeable model floc, Chem. Eng. Sci. **32**, 445 (1977).
[27] J. H. Masliyah and M. Polikar, Terminal velocity of porous spheres, Can. J. Chem. Eng. **58**, 299 (1980).
[28] J. H. Masliyah, G. Neale, K. Malysa, and T. G. M. Van De Ven, Creeping flow over a composite sphere: solid core with porous shell, Chem. Eng. Sci. **42**, 245 (1987).
[29] C. Strickland, L. Miller, A. Santhanakrishnan, C. Hamlet, N. A. Battista, and V. Pasour, Three-dimensional low Reynolds number flows near biological filtering and protective layers, Fluids **2**, 62 (2017).
[30] S. Vogel, *Life in Moving Fluids: The Physical Biology of Flow* (Princeton University Press, Princeton, New Jersey, 1996).
[31] D. Weihs and E. Barta, Comb wings for flapping flight at extremely low Reynolds numbers, AIAA J. **46**, 285 (2008).
[32] A. Santhanakrishnan, A. K. Robinson, S. Jones, A. A. Low, S. Gadi, T. L. Hedrick, and L. A. Miller, Clap and fling mechanism with interacting porous wings in tiny insect flight, J. Expt. Biol. **217**, 3898 (2014).
[33] C. N. Davies, The separation of airborne dust and particles, Proc. Inst. Mech. Eng., Part B: Manag. Eng. Manufac. **1**, 185 (1953).
[34] J. Kozeny, Ueber kapillare Leitung des Wassers im Boden. Sitzungsber Akad. Wiss., Wien **136**, 271 (1927).
[35] P. C. Carman, The determination of the specific surface of powders, I, J. Soc. Chem. Indus., Lond., Transact. **57**, 225 (1938).
[36] P. C. Carman, *Flow of Gases through Porous Media* (Academic Press, New York, 1956).
[37] A. E. Scheidegger, *The Physics of Flow through Porous Media* (University of Toronto Press, Toronto, 1974).
[38] G. G. Stokes, *On the Effect of the Internal Friction of Fluids on the Motion of Pendulums*, Vol. 9 (Pitt Press, Cambridge, 1851).
[39] R. A. Sampson, On Stokes's current function, Philos. Trans. R. Soc. London A **182**, 449 (1891).
[40] L. Squires and W. Squires, The sedimentation of thin discs, T. Am. Inst. Chem. Eng. **33**, 1 (1937).
[41] R. P. Roger and R. G. Hussey, Stokes drag on a flat annular ring, Phys. Fluids **25**, 915 (1982).
[42] A. M. J. Davis, Slow viscous flow due to motion of an annular disk; pressure-driven extrusion through an annular hole in a wall, J. Fluid Mech. **231**, 51 (1991).
[43] H. Darcy, *Les Fontaines Publique de la Ville de Dijon* (Victor Dalmont, Paris, 1856), p. 647.
[44] L. Durlofsky and J. F. Brady, Analysis of the Brinkman equation as a model for flow in porous media, Phys. Fluids **30**, 3329 (1987).
[45] S. Whitaker, Flow in porous media I: A theoretical derivation of Darcy's law, Transp. Porous Media **1**, 3 (1986).
[46] S. Whitaker, The Forchheimer equation: A theoretical development, Transp. Porous Media **25**, 27 (1996).
[47] J. Happel and H. Brenner, *Low Reynolds Number Hydrodynamics: With Special Applications to Particulate Media* (Springer Science & Business Media, The Netherlands, 2012).
[48] S. Wakiya, Viscous flows past a spheroid, J. Phys. Soc. Jpn. **12**, 1130 (1957).
[49] L. Petricca, P. Ohlckers, and C. Grinde, Micro- and Nano-Air Vehicles: State of the Art, International Journal of Aerospace Engineering **2011**, 214549 (2011).
[50] K. H. Jensen, A. X. C. N. Valente, and H. A. Stone, Flow rate through microfilters: influence of the pore size distribution, hydrodynamic interactions, wall slip, and inertia, Phys. Fluids **26**, 052004 (2014).

[51] C. Geuzaine and J.-F. Remacle, Gmsh: A 3-D finite element mesh generator with built-in pre- and post-processing facilities, Intl. J. Numer. Methods Eng. **79**, 1309 (2009).
[52] F. Hecht, New development in freefem++, J. Numer. Math. **20**, 251 (2012).
[53] H. L. Weissberg, End correction for slow viscous flow through long tubes, Phys. Fluids **5**, 1033 (1962).
[54] Z. Dagan, S. Weinbaum, and R. Pfeffer, An infinite-series solution for the creeping motion through an orifice of finite length, J. Fluid Mech. **115**, 505 (1982).
[55] S. G. E. Giap, The hidden property of Arrhenius-type relationship: Viscosity as a function of temperature, J. Phys. Sci. **21**, 29 (2010).
[56] P. E. Rueger, Liquid-liquid dispersion in batch and in-line rotor stator mixers, Ph.D. thesis, University of Maryland, College Park, 2013.
[57] Silicone fluids: stable, insert media, http://www.gelest.com/wp-content/uploads/Goods-PDF-brochures-inert_silicones_2013.pdf (unpublished).